sensors

MDPI

Article

an-QNA: An Adaptive Nesterov Quasi-Newton Acceleration-Optimized CMOS LNA for 65 nm Automotive Radar Applications

Unal Aras [1,†], Lee Sun Woo [1,†], Tahesin Samira Delwar [1], Abrar Siddique [1], Anindya Jana [2], Yangwon Lee [3,*] and Jee-Youl Ryu [1,*]

[1] Department of Smart Robot Convergence and Application Engineering, Pukyong National University, Busan 48513, Republic of Korea; unalaras21.20@gmail.com (U.A.); dltjsdn2005@gmail.com (L.S.W.); samira.fset@gmail.com (T.S.D.); abrarkhokhar.iiui@gmail.com (A.S.)
[2] Department of Electronics & Communication Engineering, JB Institute of Engineering & Technology, (Autonomous), Hyderabad 500075, India; anindya.jana@rediffmail.com
[3] Department of Spatial Information Engineering, Pukyong National University, Busan 48513, Republic of Korea
* Correspondence: modconfi@pknu.ac.kr (Y.L.); ryujy@pknu.ac.kr (J.-Y.R.)
† These authors contributed equally to this work.

Abstract: An adaptive Nesterov quasi-Newton acceleration (an-QNA)-optimized low-noise amplifier (LNA) is proposed in this paper. An optimized single-ended-to-differential two-stage LNA circuit is presented. It includes an improved post-linearization (I_{PL}) technique to enhance the linearity. Traditional methods like conventional quasi-Newton (c-QN) often suffer from slow convergence and the tendency to get trapped in local minima. However, the proposed an-QNA method significantly accelerates the convergence speed. Furthermore, in this paper, modifications have been made to the an-QNA algorithm using a quadratic estimation to guarantee global convergence. The optimized an-QNA-based LNA, using standard 65 nm CMOS technology, achieves a simulated gain of 17.5 dB, a noise figure (NF) of 3.7 dB, and a 1 dB input compression point (IP_1dB) of −13.1 dBm. It is also noted that the optimized LNA achieves a measured gain of 12.9 dB and an NF of 4.98 dB, and the IP_1dB is −17.8 dB. The optimized LNA has a chip area of 0.67 mm^2.

Keywords: adaptive Nesterov quasi-Newton acceleration (an-QNA); conventional quasi-newton (c-QN); global convergence; highly linear; low-noise amplifier (LNA); improved post-linearization (I_{PL})

Citation: Aras, U.; Woo, L.S.; Delwar, T.S.; Siddique, A.; Jana, A.; Lee, Y.; Ryu, J.-Y. an-QNA: An Adaptive Nesterov Quasi-Newton Acceleration-Optimized CMOS LNA for 65 nm Automotive Radar Applications. *Sensors* **2024**, *24*, 6141. https://doi.org/10.3390/s24186141

Academic Editor: Roman Sotner

Received: 20 August 2024
Revised: 20 September 2024
Accepted: 20 September 2024
Published: 23 September 2024

1. Introduction

A complementary metal-oxide semiconductor (CMOS) is a fundamental technology used to make integrated circuits (ICs), such as microprocessors and microcontrollers. Over the years, CMOS technology has improved tremendously. A big breakthrough in RF (radio frequency) and mixed-signal IC design came with the combination of low-noise amplifiers (LNAs) and CMOS technology [1]. The LNA is a key component of automotive radar systems. Automotive radars operate primarily at frequencies around 24 GHz [2]. Figure 1 represents the overview of RF transceiver, and Figure 2 represents the radar application.

The challenge, however, remains to design CMOS LNA for automotive radar systems. We are still in the early stages of designing and automating LNA circuits. The design of the LNA becomes more difficult when it works at high frequencies [3]. The high non-linearity of its parameters means that the researchers have a hard time designing a high-performance economic circuit on their own due to non-linearity. Additionally, the design of optimal LNAs for automotive radars is challenging because they must have wide bandwidths, low noise levels, and high linearity in order to pick up weak signals while ignoring strong ones. In order to achieve a delicate balance between these two tenets, intricate design

optimizations would be necessary along with multidisciplinary expertise in RF circuitry and multilevel considerations at the system level.

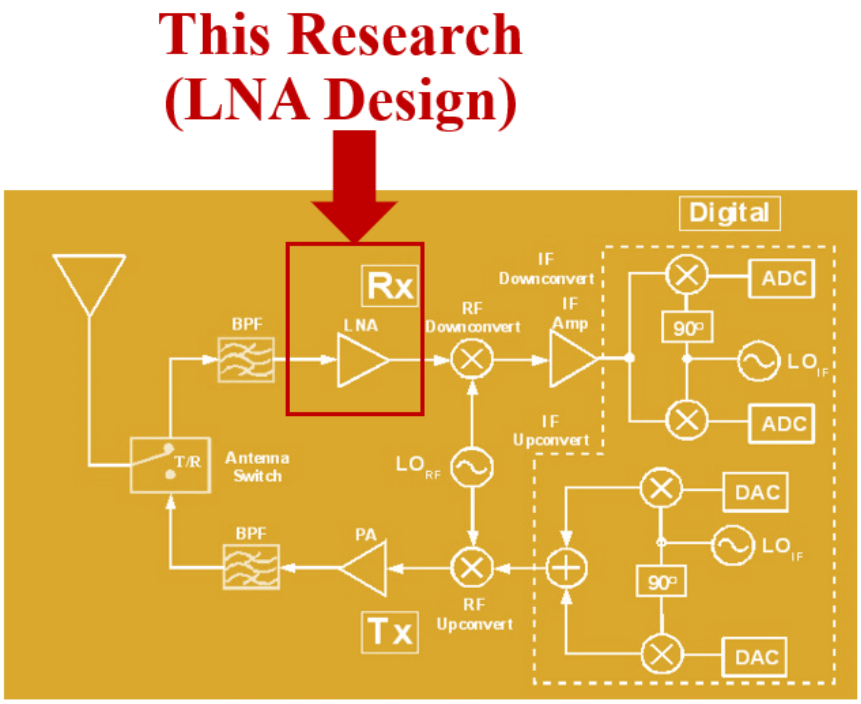

Figure 1. Overview of RF transceiver.

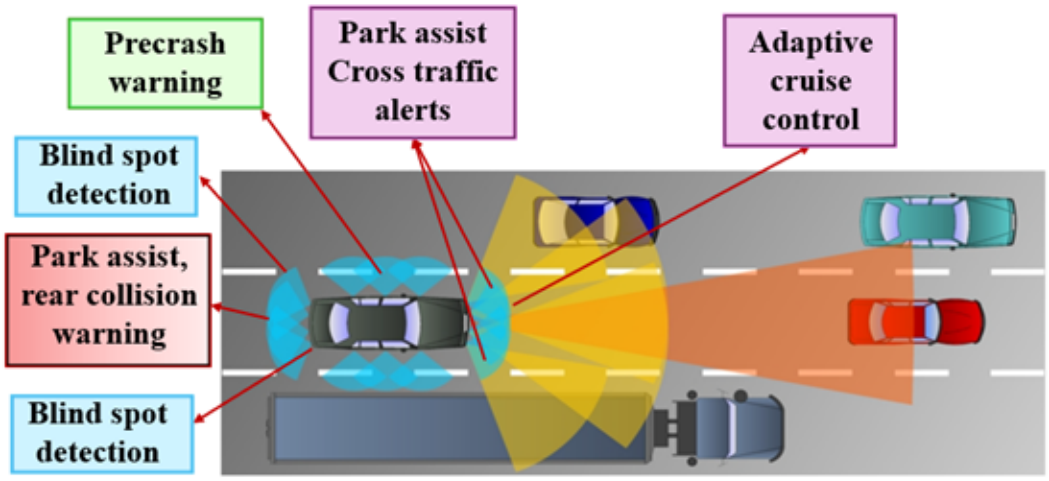

Figure 2. A 24 GHz automotive radar application.

From the prior research, it is evident that optimization algorithms (OAs) [4] play a significant role in the design process. Recent advances in intelligent paradigm research have led to a number of theoretical advancements and to successful applications of intelligent techniques and approaches to a variety of fields [5,6]. In many optimization problems, linear programming [7], Newton's method [8], gradient search methods [9], quadratic programming, and nonlinear programming [10] are used. The issue of LNA circuits has been addressed in the literature by many optimization techniques, including genetic algorithms (GA) [11], particle swarm optimization (PSO) [12], flower pollination [13], firefly algorithms (FA) [14], ant colony (AC) [15], and artificial bee colony (ABC) [16].

The PSO method was used by Thakker and Fakhfakh et al. [17,18] for the automatic sizing of low-power analog circuits, the automatic synthesis of LNA [19], and the design

of microwave filters [20]. It has been shown that a GA can be used to optimize several electrical parameters of LNAs [21]. In [22,23], for analog and RF circuit a highly efficient parasitic aware hybrid sizing methodology is proposed. According to Yiming Li et al. [24] GA generalizes the method for optimizing parameters for LNA circuits with respect to constraints. However, the paper has limitations, as using a small population size could result in unsatisfactory convergence behavior. A recent report [25,26] also noted optimized design parameters for LNAs using PSO. As demonstrated in [27], the iterative loop between the OAs and the performance evaluator allows the multi-objective artificial bee colony (MOABC) algorithm to optimize the voltage gain and noise figure.

In order to accelerate the process of convergence to the global maximum, Khong et al. [28] used direct global optimization techniques to implement a multi-unit algorithm. According to Shams et al. [29], several parameters of the LNA were optimized using GSA, including S_{21}, S_{11}, S_{22}, S_{12}, and the noise figure (NF). GSA's clustered GSA (CGSA) has been successfully exploited to reduce computational complexity, improve efficiency, and improve robustness. In [30,31], genetic computation was utilized to circumvent parasitics and achieve optimal results, but no mathematical analysis was provided. A cascade LNA was designed and optimized using PSO [32].

As part of our work, we chose adaptive Nesterov quasi-Newton acceleration (an-QNA) to optimize LNA at 24 GHz. An-QNA benefits high-frequency applications because it can be converged and optimized more quickly. With an-QNA, optimization processes are smoother, and convergence is faster. Evolutionary algorithms (EAs), however, may be preferred when the optimization is highly non-linear and non-convex or when the exploration of unconventional design spaces is required, though they may be slower to reach convergence. In contrast to conventional quasi-Newton (c-QN), which usually struggles with slow convergence and gets stuck in local minima, an-QNA guarantees faster global convergence. We have made modifications to the an-QNA algorithm to guarantee global convergence. Therefore, in the fair comparison in our work, we compare c-QN with the proposed an-QNA to optimize the 24 GHz LNA.

Main Contributions

In the following list, we summarize and discuss the paper's main contributions:

1. The paper presents an an-QNA designed to improve the performance of LNAs. The proposed an-QNA significantly accelerates the convergence speed compared to c-QN, which often suffer from slow convergence and local minima issues.
2. The proposed LNA circuit includes an improved post-linearization (I_{PL}) technique. This technique enhances the linearity of the LNA, a critical factor in achieving high-performance automotive radar applications.
3. In the proposed an-QNA, we have made modifications using a quadratic estimation to the an-QNA algorithm to ensure global convergence, addressing a significant challenge in OAs used in circuit design.
4. Utilizing standard 65 nm CMOS technology, the optimized LNA achieves a simulated gain of 17.5 dB and an NF of 3.7 dB as well as a 1 dB input compression point (IP_1dB) of −13.1 dBm. Furthermore, the optimized LNA achieves a measured gain of 12.9 dB and an NF of 4.98 dB in addition to an IP_1dB of −17.8 dB.

This paper consists of four sections. The proposed LNA circuit using an-QNA is described in Section 2. The simulation results are presented in Section 3, and in Section 4, the conclusions and future research directions are given.

2. Proposed Methodology for Optimizing an LNA Circuit

2.1. Adaptive Nesterov Quasi-Newton Acceleration (an-QNA)

an-QNA is an OA algorithm that combines the concepts of Nesterov's acceleration with quasi-Newton methods while introducing adaptivity to improve convergence speed and efficiency. c-QN methods are a class of OAs used to find the minimum (or maximum) of a function. In comparison to c-QN, the an-QNA convergence process is much faster.

2.2. Modifications in an-QNA

To achieve a faster convergence in an-QNA, we included a quadratic estimation at $w_i + \mu z_i$. Additionally, we added Nesterov's enhanced gradient, namely $\nabla F(w_i + \mu z_i)$. The an-QNA modification is briefly outlined as follows. In our work, we consider Equations (1)–(3),

$$F(w) = \frac{1}{|T_r|} \sum_{p \epsilon (T_r)} F_{p(w)} \tag{1}$$

$$F_p(w) = \frac{1}{2} \left\| d_p - o_p \right\|^2 \tag{2}$$

$$F(w) \simeq F(w_i + \mu_i z_i) + \nabla F(w_i + \mu_i)^T \nabla w + \frac{1}{2} \nabla w^T \nabla^2 F(w_i + \mu_i z_i \nabla w) \tag{3}$$

There is a precise minimization of this quadratic function in Equation (4),

$$\nabla w = -\nabla^2 F(w_i + \mu_i z_i)^{-1} \nabla F(w_i + \mu_i z_i) \tag{4}$$

It is considered as Newton's method with momentum added μz_i in Equation (5).

$$w_{i+1} = (w_i + \mu_i z_i) - \nabla^2 F(w_i + \mu_i z_i)^{-1} \nabla F(w_i + \mu_i z_i) \tag{5}$$

The inverse of Hessian in Equation (6), $\nabla F(w_i + \mu_i z_i)$ is estimated by the matrix H_{i+1},

$$\widehat{H}_{i+1} = \left((I - \widehat{\rho}_i s_i r_i^T) \widehat{H}_i \left(I - \rho_i s_i r_i^T \right) + \rho_i s_i r_i^T \right) \tag{6}$$

where

$s_i = w_{i+1} - (w_i + \mu_i z_i)$

$r_i = \nabla F(w_{i+1}) - \nabla F(w_i + \mu_i z_i)$,

Then, the renew vector of an-QNA can be written as in Equations (7) and (8),

$$z_{i+1} = \mu_i z_i - \alpha_i \widehat{g}_i \tag{7}$$

$$\widehat{g}_i = -\widehat{H}_i \nabla F(w_i z_i) \tag{8}$$

Thus, the vector in the modified method is given as in Equations (9) and (10),

$$\widehat{\xi}_i = w \parallel \nabla F(w_i + \mu z_i) \parallel + max \left\{ \frac{-\epsilon_i^T s_i}{\parallel s_i \parallel^2, 0} \right\} \tag{9}$$

$$\begin{Bmatrix} \omega = 2 & if \parallel \nabla F(w_i + \mu z_i \parallel^2 > 10^{-2}) \\ \omega = 100 & if \parallel \nabla F(w_i + \mu z_i \parallel^2 < 10^{-2}) \end{Bmatrix} \tag{10}$$

Figure 3 presents the training error vs. iteration counts of LNA, while Figure 4 shows LNA training error vs. time. Table 1 presents the summary of the simulation results of LNA modeling. From Table 1, we can see that the convergence rate for c-QN is 75% while the convergence rate of the proposed an-QNA is 100%. On the other hand, the c-QN's execution time is 65 s, and the proposed an-QNA's execution time is 95 s.

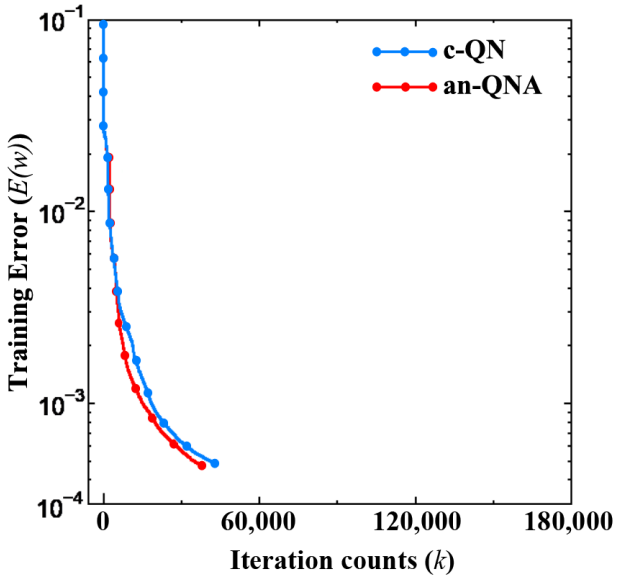

Figure 3. The training error vs. iteration counts of LNA.

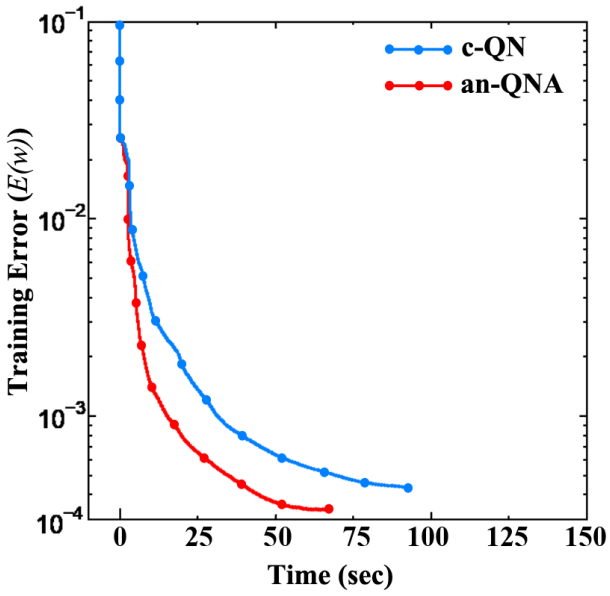

Figure 4. The training error vs. time of LNA.

Table 1. Summary of the simulation results of LNA modeling.

Name of Algorithm	$\text{Training}_{\text{Error}}$ Median/Ave/Best/Worst (w) ($\times 10^{-3}$)	Iteration Counts (k)	Time (s)	$\text{Test}_{\text{Error}}$ Median/Ave/Best/Worst (w) ($\times 10^{-3}$)	Rate of Convergence (%)
c-QN	0.75/0.76/0.62/0.91	41,828	95	0.640/0.901/0.534/2.01	75%
an-QNA	0.57/0.51/0.32/0.65	35,561	65	0.798/1.14/0.591/2.15	100%

2.3. Convergence Performance Analysis of an-QNA

In this section, Equations (11)–(18) represent eight benchmark functions, both unimodal and multimodal, which are employed to assess the performance of the an-QNA algorithm. Table 2, provides detailed information regarding the dimensions, minimum range, and function characteristics of these benchmark functions. The performance of gradient-based OAs such as c-QN and adaptive moment estimation (ADAM) has been

evaluated alongside the an-QNA variant to examine aspects like convergence rate, stability, and computational accuracy across multiple iterations, as depicted in Figure 5. The results demonstrate that, when comparing the optimal function values plotted over several generations in Figure 5, the an-QNA variant outperforms others in terms of convergence, particularly in scenarios with models of varying sizes, ranging from 1000 to 5000 dimensions. The graphs indicate that for the an-QNA variants, the standard test function values decrease rapidly as the number of generations increases, in contrast to other OAs. In Figure 5, it can be observed that both c-QN and ADAM exhibit slow convergence and tend to stagnate during the partitioning process. However, the an-QNA variant, particularly in terms of the mean strategy, effectively prevents the algorithm from getting trapped in local minima and enhances the search process by speeding up convergence.

$$Function_{v1-unimodal}(y) = \sum_{i=1}^{n} y_i^2 \tag{11}$$

$$Function_{v1-unimodal}(y) = \sum_{i=1}^{n} \left(\sum_{j-1}^{n} y_j \right)^2 \tag{12}$$

$$Function_{v3-unimodal}(y) = \sum_{i=1}^{n} \left[(y_i + 0.5)^2 \right] \tag{13}$$

$$Function_{v4-unimodal}(y) = \sum_{i=1}^{n} i y_i^4 + rand[0,1] \tag{14}$$

$$Function_{v5-multimodal}(y) = \sum_{i=1}^{n} -y_i sin\left(\sqrt{|y_i|} \right) \tag{15}$$

$$Function_{v6-multimodal}(y) = -20exp\left(-0.2\sqrt{\frac{1}{n}\sum_{i=1}^{n} y_i^2} - exp\left(\frac{1}{n}\sum_{i=1}^{n} cos(2\pi y_i) \right) + 20 + e \right) \tag{16}$$

$$Function_{v7-multimodal}(y) = \sum_{i=1}^{n} \left[y_i^2 - 10cos(2\pi y_i) \right] + 10 \tag{17}$$

$$Function_{v8-multimodal}(y) = \sum_{i=1}^{n} \left[y_i^2 - 10cos(2\pi y_i) \right] + 10 \tag{18}$$

$$Function_{v8-multimodal}(y) = \frac{1}{4000}\sum_{i=1}^{n} - \prod_{i=1}^{n} cos\left(\frac{y_i}{\sqrt{i}} + 1 \right) \tag{19}$$

Table 2. Multimodal and unimodal benchmark functions (dimensions, minimum range).

Function Name	Dimension	Range	Minimum Function (fmin)
$Function_{v1(unimodal)\ (y)}$	30	[−100, 100]	0
$Function_{v2(unimodal)\ (y)}$	30	[−100, 100]	0
$Function_{v3(unimodal)\ (y)}$	30	[−100, 100]	0
$Function_{v4(unimodal)\ (y)}$	30	[−1.28, 1.28]	0
$Function_{v5(multimodal)\ (y)}$	30	[−500, 500]	-418.9×5
$Function_{v6(multimodal)\ (y)}$	30	[−32, 32]	0
$Function_{v7(multimodal)\ (y)}$	30	[−5.1, 5.1]	0
$Function_{v8(multimodal)\ (y)}$	30	[−600, 600]	0

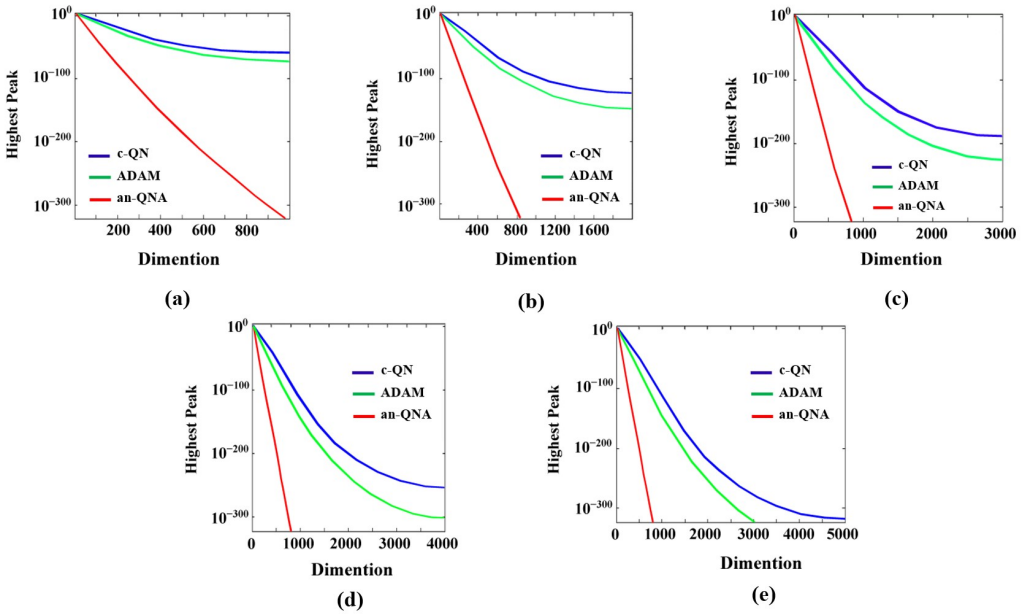

Figure 5. Convergence graphs of c-QN, ADAM, an-QNA algorithms (**a**) 1000 dimension (**b**) 2000 dimension (**c**) 3000 dimension (**d**) 4000 dimension (**e**) 5000 dimension.

The c-QN, ADAM, and an-QNA algorithms were developed using MATLAB R2021a. Tables 3–5 indicate that the c-QN, ADAM, and an-QNA algorithms deliver the best optimal values for classical optimization problems in terms of the minimum and maximum function values compared to other OAs. Meanwhile, Tables 6–8 show that the an-QNA outperforms c-QN and ADAM in terms of producing higher-quality standard and mean values for most classical functions, yielding the smallest function values. Additionally, the convergence graphs in Figures 6 and 7 demonstrate that an-QNA achieves the best possible optimal values for standard functions in fewer iterations than c-QN and ADAM. The results presented in Tables 6–8 clearly show that the proposed an-QNA variant surpasses the performance of other algorithms, including c-QN and ADAM, in terms of mean, standard deviation, and minimum/maximum cost function values while efficiently finding the optimum. Therefore, the an-QNA variant proves to be highly competitive with other OAs.

Furthermore, the convergence behaviors of c-QN, ADAM, and the proposed an-QNA algorithms have been analyzed, with the convergence curves depicted in Figures 6 and 7. These curves reveal that the an-QNA consistently achieves better convergence points than the other algorithms. The obtained results confirm that the an-QNA is more effective in identifying the best optimal solution with fewer iterations. As a result, the an-QNA algorithm successfully avoids premature convergence to local optima and enhances the exploration of the search space.

Table 3. The c-QN best solutions and statistical outcomes (unimodal benchmark functions).

	Minimum	Maximum	μ	α
c-QN	6.16×10^{-61}	5.8×10^{4}	215.8	2.5×10^{3}
	1.97×10^{-35}	1.43×10^{12}	1.43×10^{9}	4.52×10^{10}
	3.3×10^{-15}	1.8876×10^{5}	1.7745×10^{3}	1.0505×10^{4}
	2.6647×10^{-14}	89.07	2.61	12.13
	27.11	2.1621×10^{8}	7.4518×10^{5}	1.0897×10^{7}
	1.2547	6.5240×10^{4}	335.9	3.4849×10^{3}
	3.61×10^{-4}	92.21	0.49	5.80

Table 4. The ADAM best solutions and statistical outcomes (unimodal benchmark functions).

	Minimum	Maximum	μ	α
ADAM	2.71×10^{-73}	6.15×10^{4}	173.1716	2.53×10^{3}
	7.42×10^{-43}	3.2669×10^{9}	3.2708×10^{6}	1.03×10^{8}
	2.52×10^{-25}	1.1651×10^{5}	674.7361	5.80×10^{3}
	2.42×10^{-20}	88.03	0.945	6.765
	27.16	2.30×10^{8}	6.71×10^{5}	9.98×10^{6}
	1.25	7.07×10^{4}	197.70	2.81×10^{3}
	5.791×10^{-4}	80.65	0.133	2.668

Table 5. The an-QNA best solutions and statistical outcomes (unimodal benchmark functions).

	Minimum	Maximum	μ	α
an-QNA	0.00	7.10×10^{4}	125.5	2.4×10^{3}
	1.60×10^{-175}	3.78×10^{13}	1.27×10^{10}	1.1956×10^{12}
	1.2×10^{-282}	6.174×10^{4}	1.2536×10^{3}	1.0787×10^{4}
	1.7×10^{-152}	88.03	0.349	4.369
	27.10	2.30×10^{8}	3.5409×10^{5}	1.00×10^{7}
	3.87	7.07×10^{4}	123.81	2.5129×10^{3}
	1.41×10^{-5}	80.652	0.202	4.97

Table 6. The c-QN best solutions and statistical outcomes (multimodal benchmark functions).

	Minimum	Maximum	μ	α
c-QN	-5.80×10^{3}	-2.44×10^{3}	-4.03×10^{3}	967.79
	5.68×10^{-14}	458.78	10.78	48.011
	1.50×10^{-14}	20.7623	0.412	2.276
	0.009	665.77	3.149	32.93
	0.03	5.520×10^{8}	1.57×10^{6}	2.49×10^{7}
	0.69	8.056×10^{8}	3.20×10^{6}	4.36×10^{7}

Table 7. The ADAM best solutions and statistical outcomes (multimodal benchmark functions).

	Minimum	Maximum	μ	α
ADAM	-4.8344×10^{3}	-2.5399×10^{3}	-3.3352×10^{3}	731.9012
	0	438.1148	4.9465	32.6783
	1.5099×10^{-14}	20.7623	0.2497	1.7307
	0	527.3462	1.4174	20.4885
	0.0538	6.1414×10^{8}	1.1003×10^{6}	2.1982×10^{7}
	1.11284	9.0172×10^{8}	1.5261×10^{6}	3.2837×10^{7}

Table 8. The an-QNA best solutions and statistical outcomes (multimodal benchmark functions).

	Minimum	Maximum	μ	α
an-QNA	-2.25×10^{3}	-2.23×10^{3}	-2.25×10^{3}	6.3372
	0	488.07	2.33	26.43
	1.4×10^{-15}	20.8472	0.1045	1.1726
	0	555.03	0.959	18.93
	0.558	8.105×10^{8}	1.04×10^{6}	2.15×10^{7}
	0.193	9.23×10^{8}	1.103×10^{6}	2.9672×10^{7}

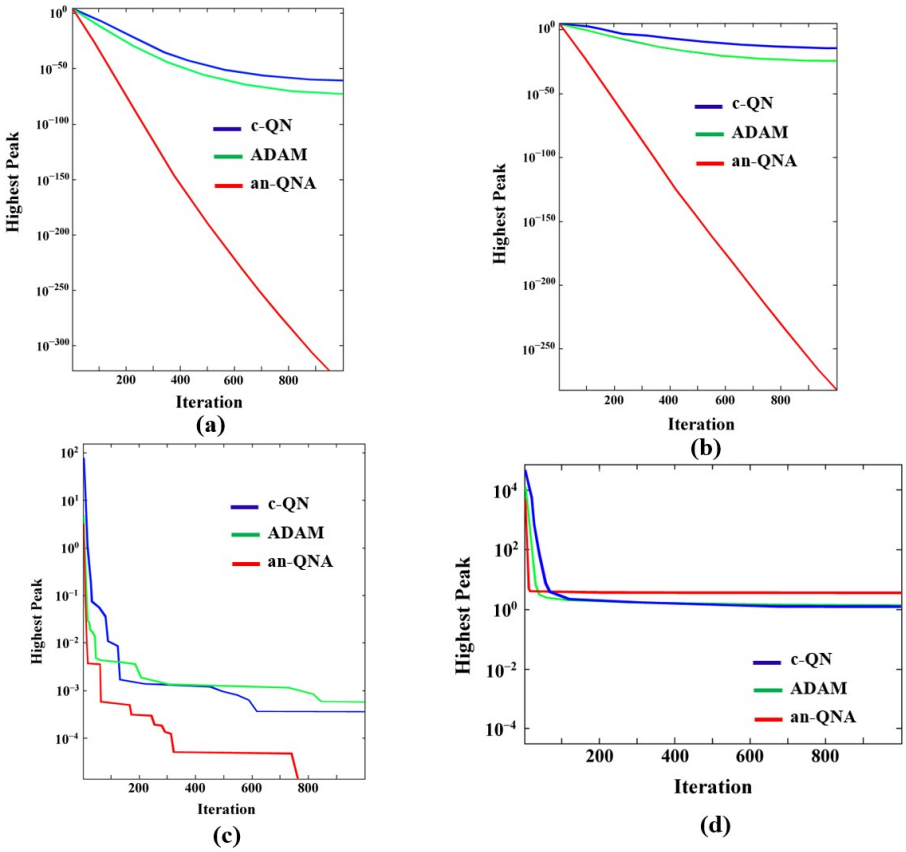

Figure 6. Convergence graph of unimodal benchmark functions (**a**) F_{v1} (**b**) F_{v2} (**c**) F_{v3} (**d**) F_{v4}.

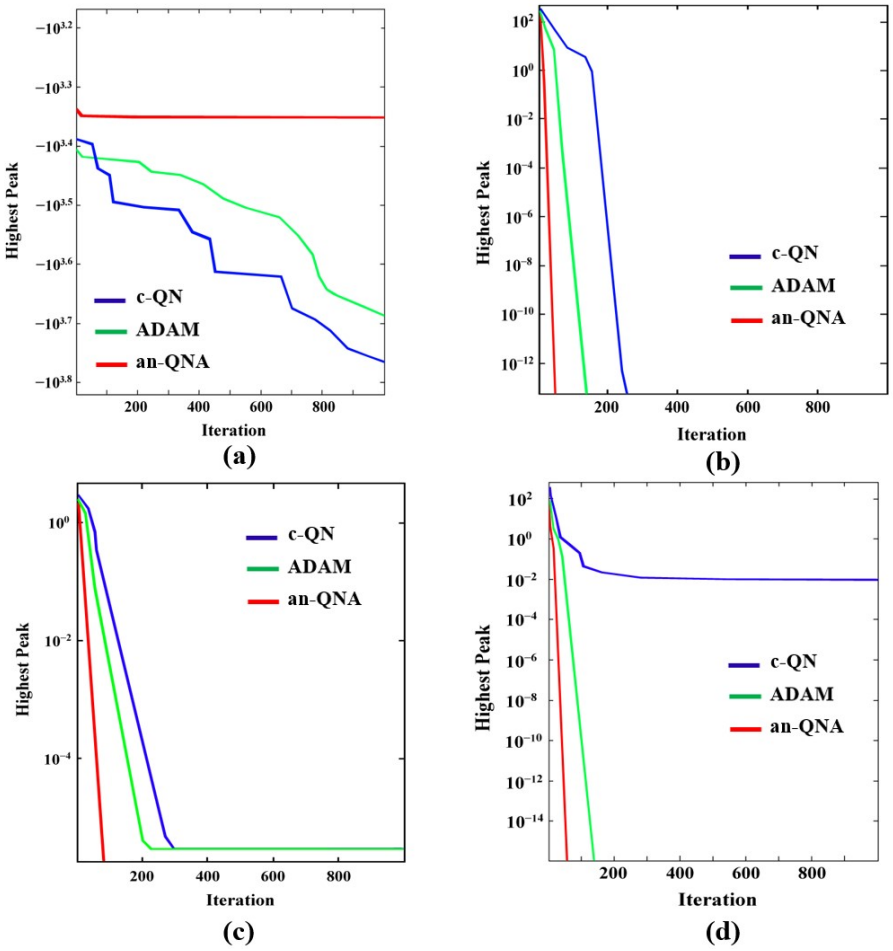

Figure 7. Convergence graph of multimodal benchmark functions (**a**) F_{v5} (**b**) F_{v6} (**c**) F_{v7} (**d**) F_{v8}.

3. Proposed an-QNA Based LNA Circuit

The schematic of the proposed single-ended-to-differential LNA using an-QNA is shown in Figure 8. The designed LNA is composed of two stages. The first stage includes the transistor in a common-source configuration, and the second stage of the LNA includes a common-source transistor cascoded with a common-gate transistor. An improved post-linearization (I_{PL}) technique is implemented to mitigate the non-linearity of the designed LNA. Table 9 shows the proposed LNA device component values using an-QNA.

Table 9. Proposed LNA device component values using an-QNA.

Element	Dimension
M_1	32 µm/65 nm
M_2	54 µm/65 nm
M_3	54 µm/65 nm
C_1, C_2, C_3	1 pF, 4.2 pF, 1.2 pF
$L_1 \sim L_3$	1.3 nH, 1.5 nH, 170 pH
$L_4 \sim L_6$	1.5 nH, 1.8 nH, 154 pH

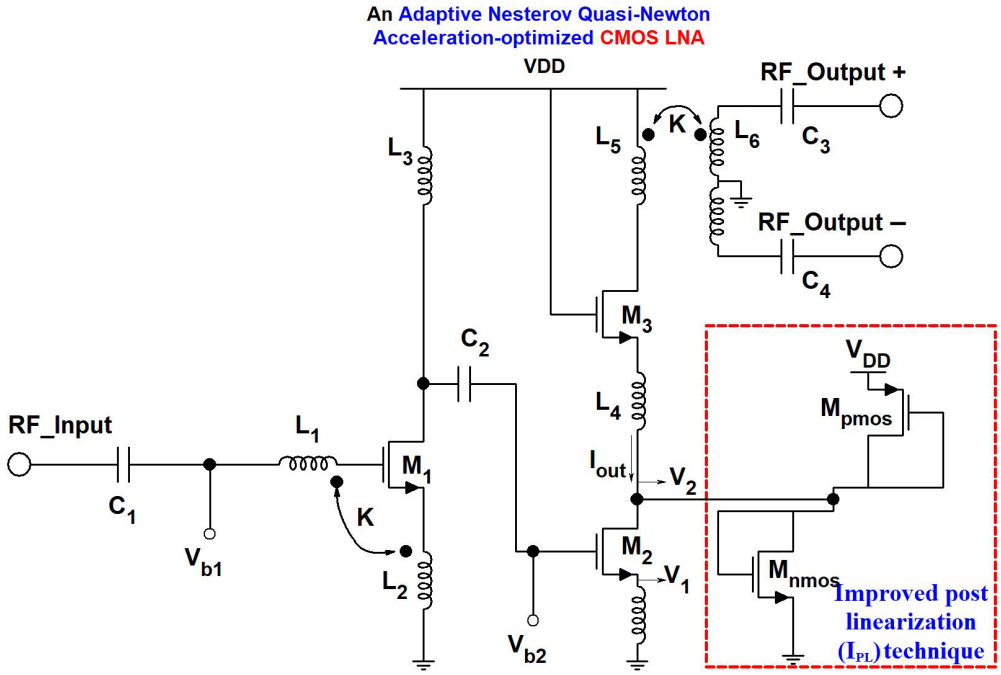

Figure 8. Proposed two-stage LNA using an-QNA.

An input matching of the designed LNA consists of a feedback transformer formed by the coupling of L_1 and L_2. The input impedance of the amplifier is approximately given by Equation (20):

$$Z_{in} \approx \frac{1}{g_m} \frac{\left(\frac{n}{k}\right)^2}{\frac{n}{k}+1} \tag{20}$$

where g_m refers to the transconductance of the transistor M_1,

$$n = \sqrt{\frac{L_1}{L_2}} \tag{21}$$

Here, n is the turns ratio, and k is the coupling factor. The input matching is shown by Equation (21) and is frequency independent, which means ideally the input match is wideband. Thus, as the transformer layout has parasitic capacitances that depend on frequency and change over frequency, it limits the input-matching bandwidth. The use of a transformer-based matching technique is beneficial over traditional lumped components matching because it is wideband, and wideband is needed to meet the input return loss (S_{11}) specification of −10 dB over the interested frequency band. The optimal sizing and biasing for the first-stage common-source transistor is selected for its minimal noise. Figure 9 shows the plot of the minimum noise NF_{min} versus the bias current of the M_1 transistor of width 32 µm and gate length 65 nm. It shows that an NF_{min} of 0.5 dB at 0.5 mA can be achieved.

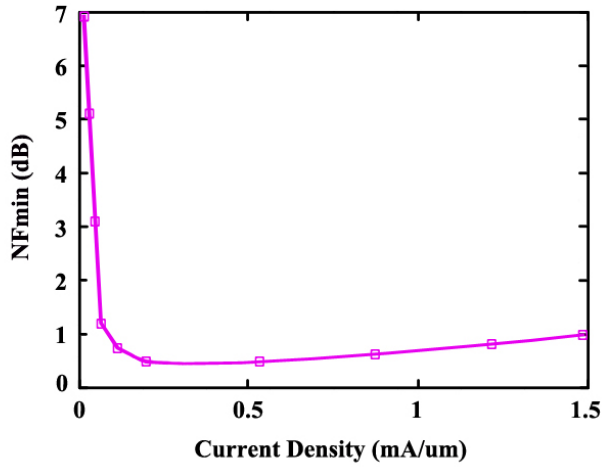

Figure 9. NF_{min} vs. current density.

Linearity Analysis

A list of distortion sources and linearization methods is presented in Table 10. From the table, we can determine that, in most reported linearization techniques, distortion of transconductance is suppressed at the 2nd and 3rd orders. In light of this, linearization of higher-order terms (beyond the third order) as well as output conductance remain open issues. Typically, the non-linearity in LNA arises because of the non-linear behavior of currents of transistors. In this work, to solve the non-linearity issue, rather than using the above-mentioned conventional technique, we have used a I_{PL} technique to increase the linearity.

Table 10. An description of distortion sources and linearization methods [33].

Distortion Sources	**g_m**				**g_{ds}**
Methods of Linearization	**Intrinsic 2nd Order**	**Intrinsic 3rd Order**	**2nd-Order Interaction**	**Higher Order**	
Feedback	✓	✓		✓	
Harmonic termination		✓	✓		
Optimal biasing		✓			
Feedforward	✓	✓		✓	
Derivative superposition (DS)		✓			
Complementary DS	✓	✓			
Differential DS	✓	✓			
Modified DS		✓	✓		
IM2 injection		✓	✓		
Noise/distortion cancellation	✓	✓			✓
Post-Distortion	✓	✓			

In our circuit, the inductor L_4 is connected between the drain and source of transistor M_2, M_3, and the parasitic capacitances at the source of M_3 and at the drain M_2 form a

wideband π network. The proper sizing of L_4 cancels the parasitic capacitive effects, which forms a short circuit over the whole frequency on interest. In this state, nonlinearity from transistor M_3 can be ignored [34], which leaves the transistor M_2 as the main source of non-linearity. The implemented I_{PL} technique facilitates partially canceling the second-order and third-order non-linearity, which can be analyzed by using the Taylor series expressions of the drain currents I_2 of transistors M_2, I_{nmos} of transistors M_{nmos}, and I_{pmos} of transistors M_{pmos}.

$$i_2 = g_{m1}v_1 + g_{m1}v_1^2 + g_{m3}v_1^3 \tag{22}$$

$$i_{nmos} = g_{mn1}v_2 + g_{mn2}v_2^2 + g_{mn3}v_2^3 \tag{23}$$

$$i_{pmos} = g_{mp1}v_2 + g_{mp2}v_2^2 + g_{mp3}v_2^3 \tag{24}$$

$$v_2 = b_1v_1 + b_2v_1^2 + b_3v_1^3 \tag{25}$$

where b_1–b_3 are, in general, frequency dependent. In practice, the π network cancels the effects of b_2 and b_3 at the frequency of interest formed by the inductor L_4 and the parasitic capacitances at the drain of M_2 and at the source M_3.

$$\begin{aligned} i_{out} &= i_2 + i_{nmos} + i_{pmos} \\ &= \left[g_{m1} - b_1\left(g_{mn1} + g_{mp1}\right)\right]v_1 + \left[g_{m2} - b_2\left(g_{mn1} + g_{mp1}\right)\right] \\ &+ b_1^2\left(g_{mn2} + g_{mp2}\right) + \left[g_{m3} - b_3\left(g_{mn1} + g_{mp1}\right) + b_1^3\left(g_{mn3} + g_{mp3}\right) + 2b_1b_2\left(g_{mn2} + g_{mp2}\right)\right]v_1^3 \end{aligned} \tag{26}$$

The third-order non-linearity of the Iout (third term in (Equation (26))) should be zero or close to zero in order to attain a better IIP3. The I_{PL} technique uses voltage V_2 and duplicates the non-linear drain current of transistor M_2, partially canceling both second-order and third-order distortion terms. Finally, M_2, M_n, and M_p use the same finger sizes to improve matching and, hence, the cancellation of harmonics. The relationship between the M_2 source voltage V_1, M_2 drain voltage V_2, and the input voltage V_{in} at the gate of transistor M_2 can be stated up to the third order in Equation (27), while the expression of IIP3 is calculated as shown in Equation (28):

$$V_1 = A_1(\omega)oV_{in} + A_2\left(\omega_1\omega_2oV_{in}^2 + C_3\left(\omega_{1,}\omega_{2,}\omega_{3,}oV_{in}^3\right)\right) \tag{27}$$

$$IIP3 = 20.log_{10}\left(\sqrt{\left|\frac{4}{3}.\frac{C_1(\omega)}{C_3(\omega_1,\omega_2,\omega_3)}\right|}\right) + 10\text{dB} \tag{28}$$

where "o" is the Volterra series operator [35]. $C_1(\omega)$ is usually fixed by the design parameters; therefore, low distortion is achieved by reducing $C_3(\omega_1, \omega_2, \omega_3)$. The MOS transistor operated in saturation region exhibits third-order negative transconductance and second-order positive transconductance, so concurrently decreasing the second- and third-order transconductance increases IIP3. The simulated results of IIP3 vs. frequency with and without implemented I_{PL} are shown in Figure 10.

Figure 11 depicts that the flowchart of the proposed LNA using the an-QNA algorithm begins with the design process initiation, where the optimized LNA circuit is developed using the an-QNA method. The first step is selecting the 65 nm CMOS technology, which serves as the basis for the LNA fabrication. Next, the single-ended-to-differential two-stage LNA circuit block is designed, establishing the core structure. Transistor devices and lumped components, such as resistors and capacitors, are then sized according to the performance needs. The an-QNA algorithm is applied to optimize key parameters like gain, NF, and output power, with modifications to guarantee global convergence through quadratic estimation. The performance of the LNA is subsequently evaluated, and if the specifications (such as gain, NF, and linearity) are met, then the design moves forward. If not, further optimization is performed. Finally, once all performance criteria are satisfied, the optimal values for the transistors and components are finalized, completing the design process of the LNA using the an-QNA method.

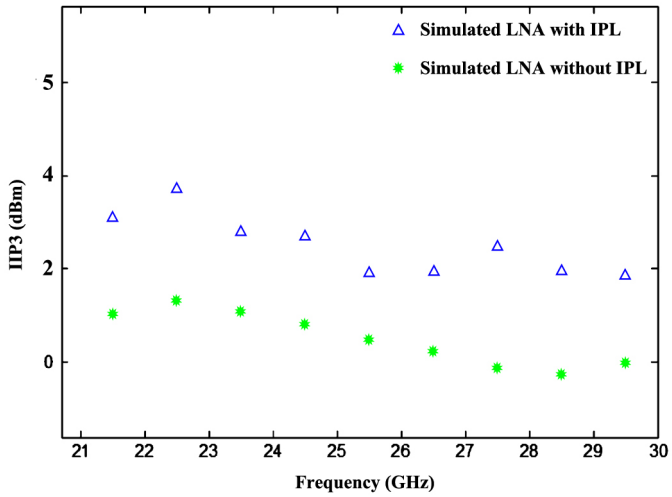

Figure 10. IIP3 vs. frequency.

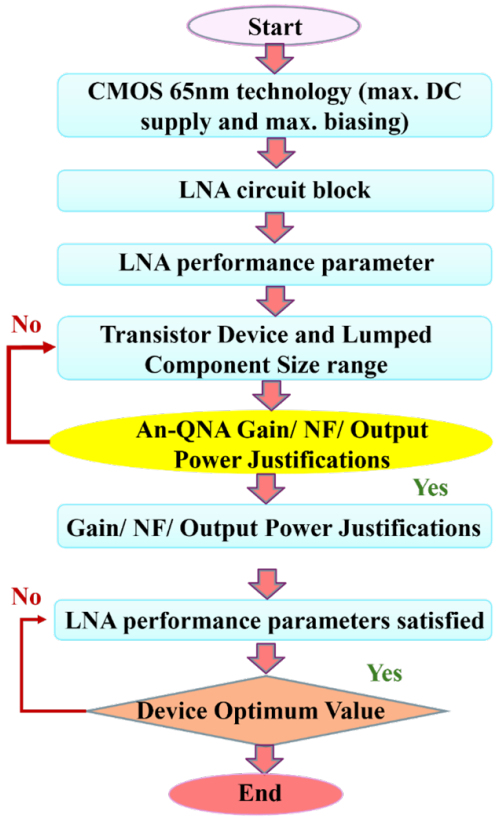

Figure 11. Flowchart of the proposed LNA using an-QNA.

4. Results and Discussion

An LNA based on the proposed design is simulated on CMOS with 65 nm. The proposed an-QNA-based optimized LNA consumes 28 mW of power and operates at 1.8 volts.

Figure 12 presents the simulated gain S_{21} of the proposed LNA (using an-QNA c-QN and, w/o optimization). In an-QNA, the simulated gain S_{21} is 17.5 dB, while in c-QN, it is 15 dB. A 13.9 dB simulated gain S_{21} without optimization is also achieved.

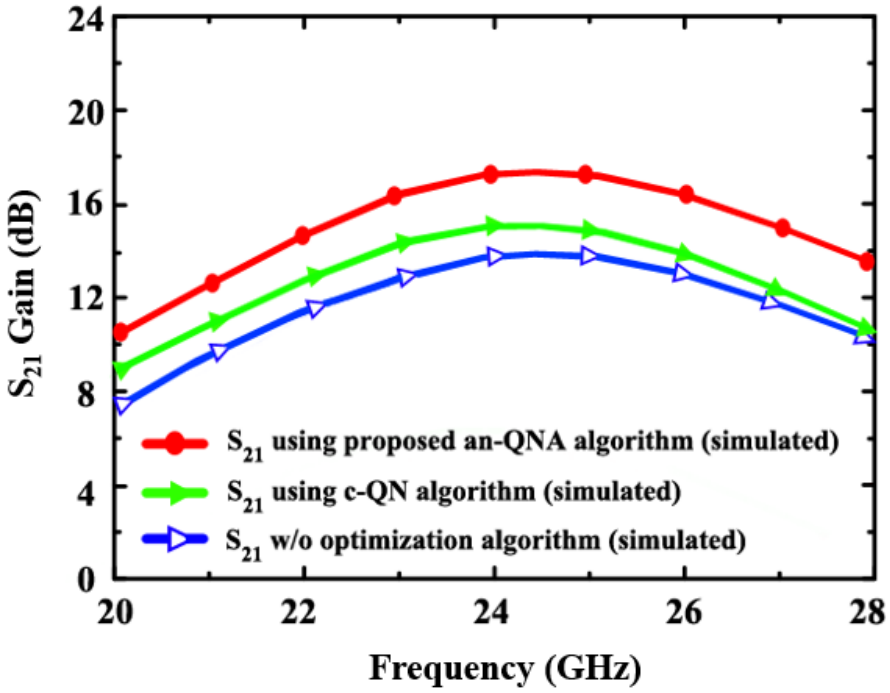

Figure 12. The simulated gain S_{21} of the proposed LNA (using an-QNA and c-QN and without optimization).

In Figure 13, the simulated and measured gain S_{21} of the proposed LNA (using an-QNA) is shown. According to the simulation, the measured one is 12.9 dB, while the simulated one is 17.5 dB.

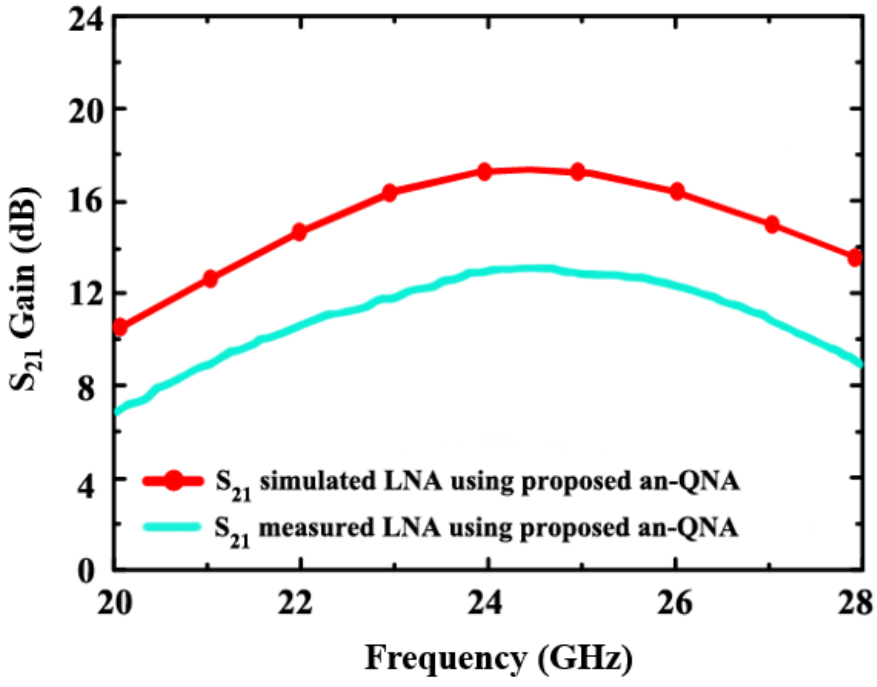

Figure 13. The simulated and measured gain S_{21} of the proposed LNA (using an-QNA).

In Figures 14 and 15, the simulated S_{22} and S_{11} for the proposed LNA (using an-QNA and c-QN and without optimization) is illustrated. The S_{11} simulation results are −9.1 dB,

−10.9 dB, and −11.7 dB, and those for S_{22} (an-QNA and c-QN without optimization) are −8 dB, −9.8 dB, and −10.2 dB, respectively.

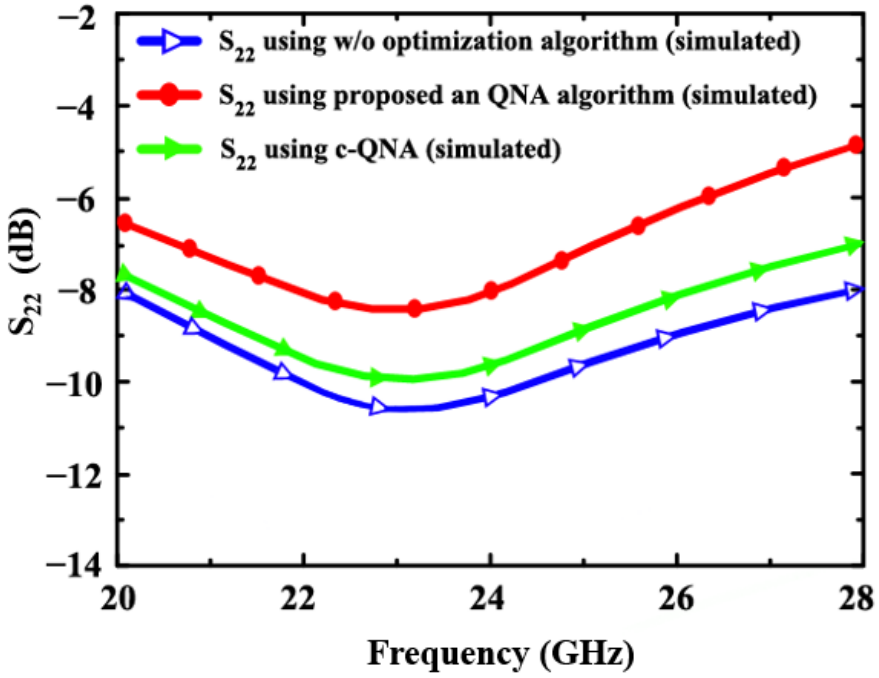

Figure 14. The simulated S_{22} of the proposed LNA (using an-QNA c-QN and, w/o optimization).

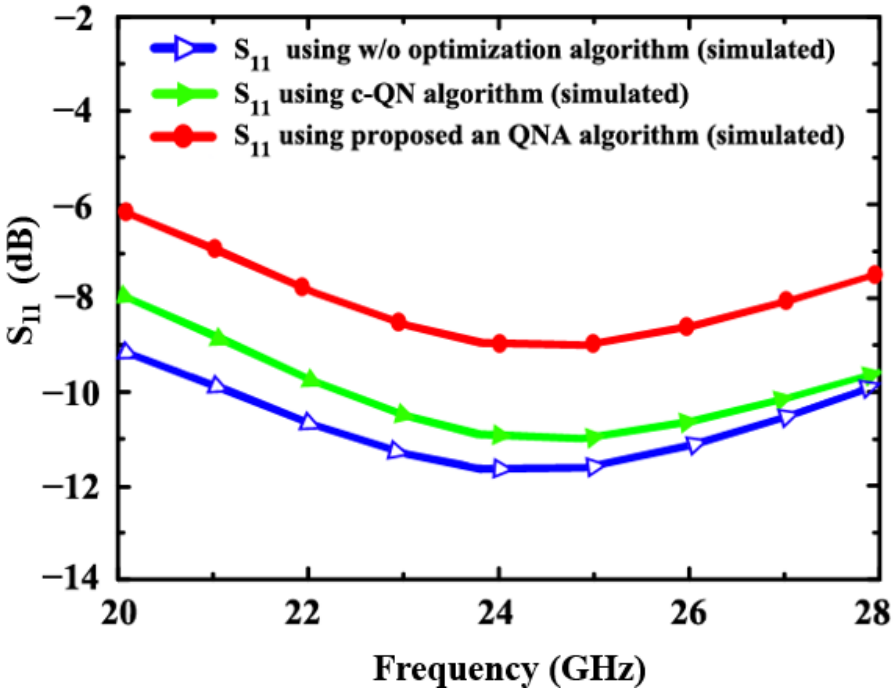

Figure 15. The simulated S_{11} of the proposed LNA (using an-QNA c-QN and, w/o optimization).

Figures 16 and 17 demonstrate the simulated NF and measured NF of the proposed LNA (using an-QNA and c-QN and without optimization). The simulated NF is 3.7 dB, but the measured NF is 4.98 dB.

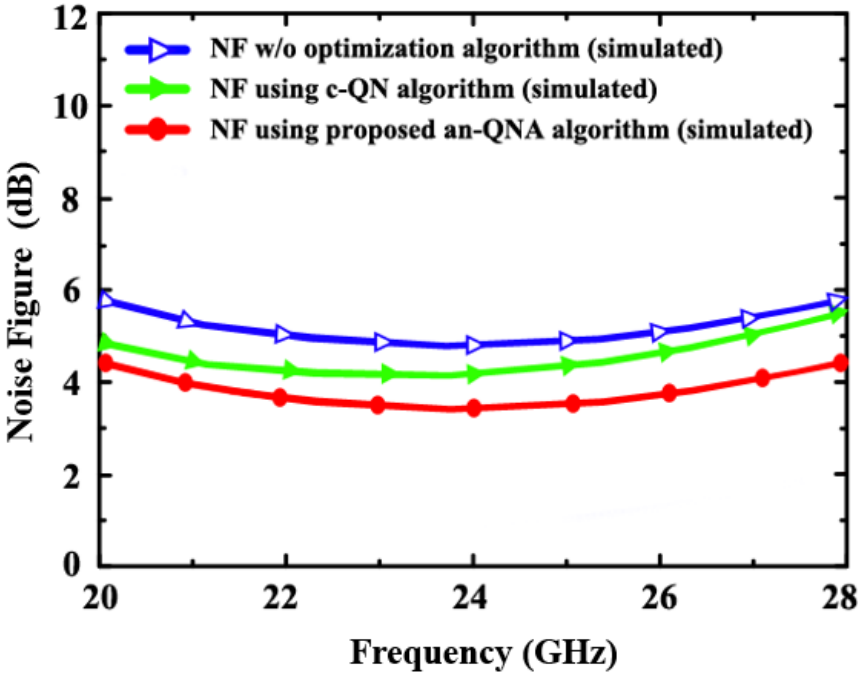

Figure 16. The simulated NF of the proposed LNA (using an-QNA and c-QN and without optimization).

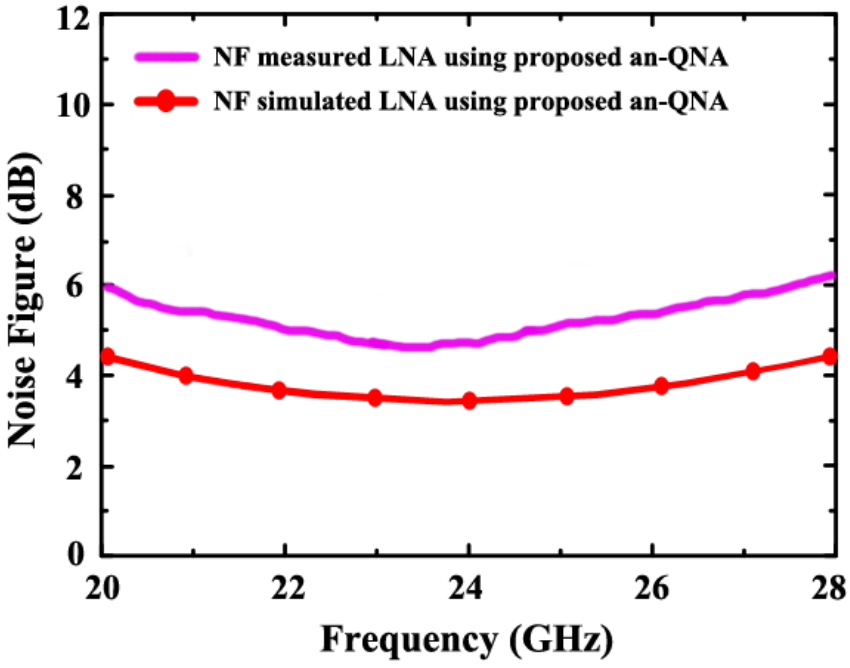

Figure 17. The simulated and measured NF (using an-QNA).

Figure 18 depicts the simulated IP_1dB of the proposed LNA (using an-QNA). In simulations, the IP_1dB of an LNA based on a QNA is achieved at −13.1 dB.

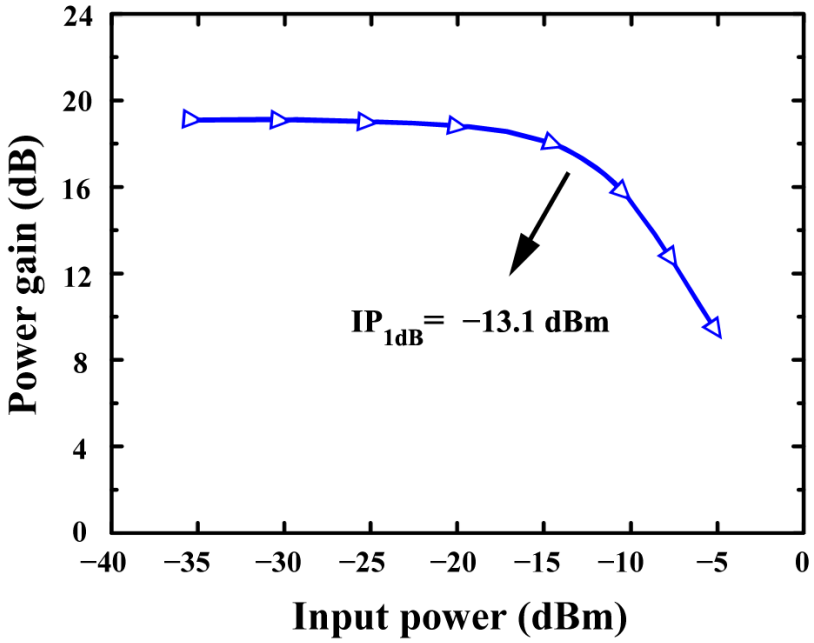

Figure 18. The simulated IP_1dB of the proposed LNA (using an-QNA).

According to Figure 19, the proposed LNA's IP_1dB is simulated using c-QN. Based on simulations, an LNA using c-QN achieves −15.2 dB IP_1dB.

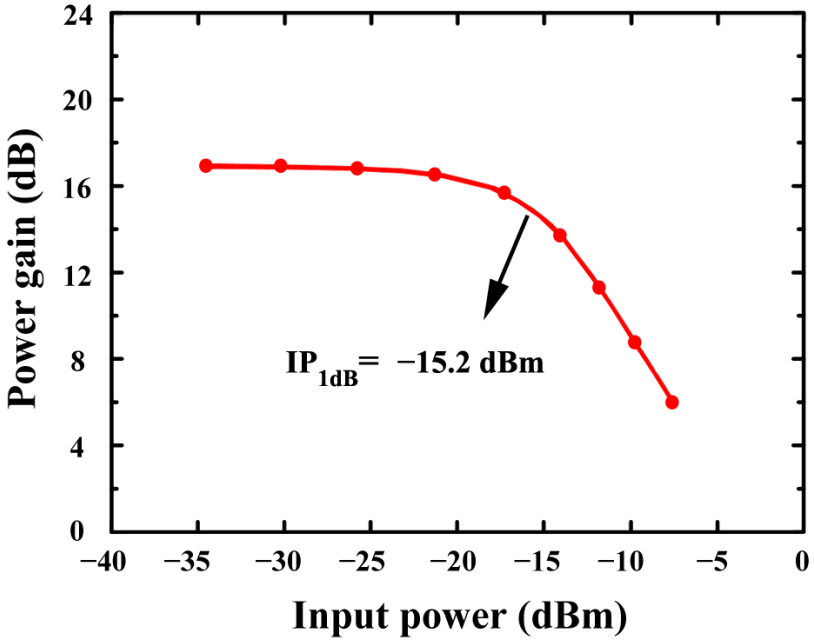

Figure 19. The simulated IP_1dB of the proposed LNA (using c-QN)).

Figure 20 illustrates the simulated IP_1dB of the proposed LNA (without optimization). The LNA without optimization has an IP_1dB of −16.1 dB in simulations.

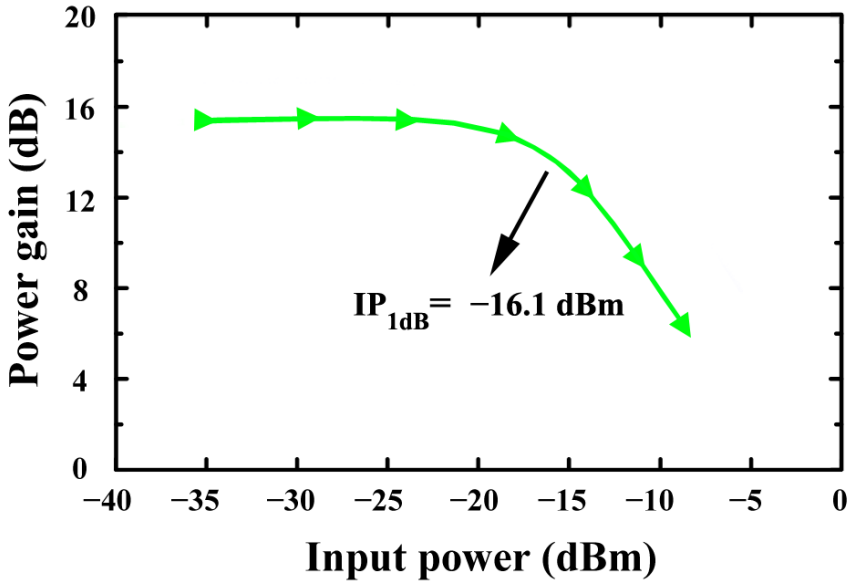

Figure 20. The simulated IP_1dB of the proposed LNA (without optimization).

Figure 21 depicts the simulated and measured IP_1dB of the proposed LNA (using an-QNA). In simulations, the IP_1dB of an LNA based on an-QNA is −13.1 dB, while measured one is −17.5 dB.

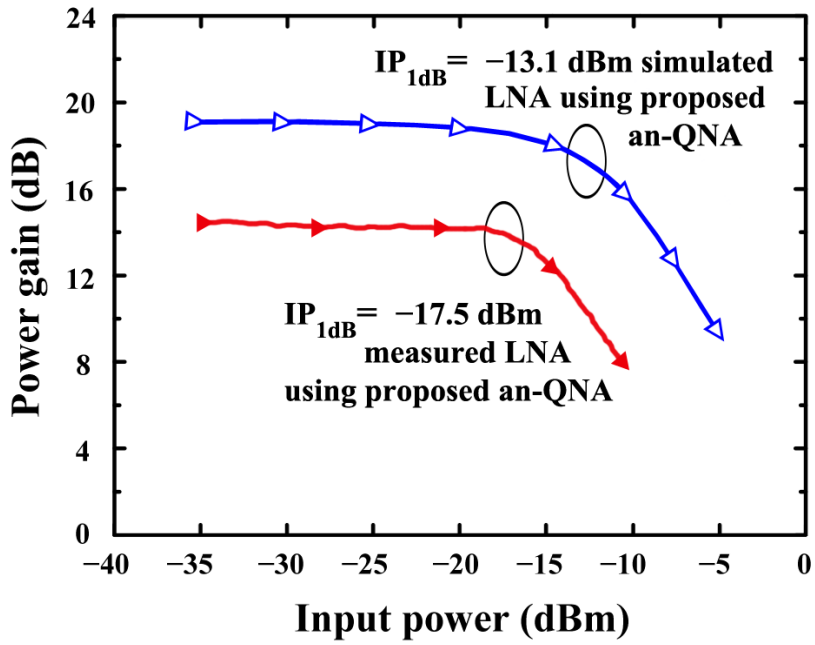

Figure 21. The measured and simulated IP_1dB of the proposed LNA (using an-QNA).

Figure 22 illustrates the NF characteristics at different supply voltages (Vdd). The NF reaches a maximum value of 3.7 dB at 24 GHz when operating at 1.8 V, while it decreases to a minimum of 3 dB when the supply voltage is increased to 2.0 V. Figure 23 shows the variation in S_{21} across different voltages. At 1.8 V, the S_{21} achieves 17.5 dB, and as the voltage increases, S_{21} improves further, reaching 18 dB at 1.9 V and 18.9 dB at 2.0 V.

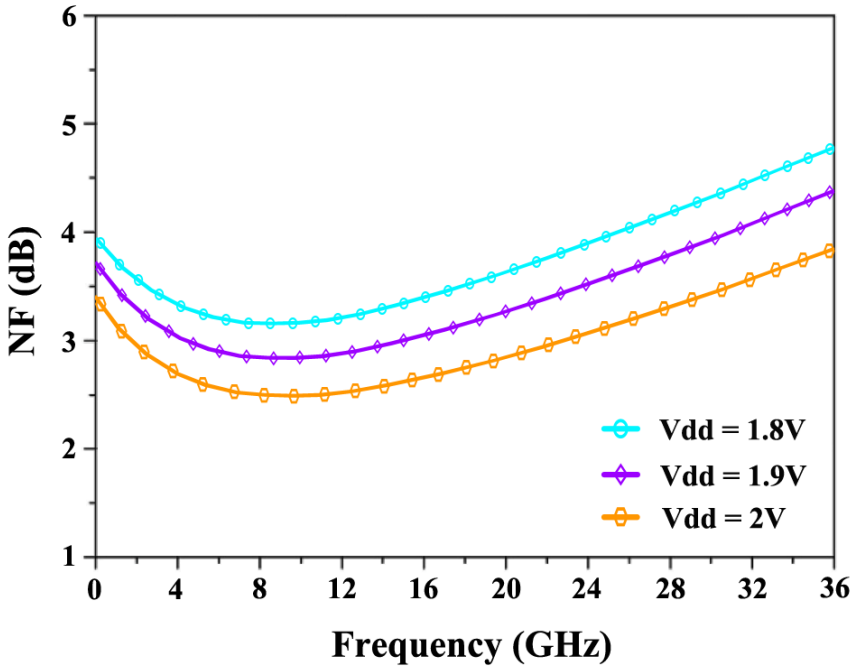

Figure 22. NF's response to power supply variations.

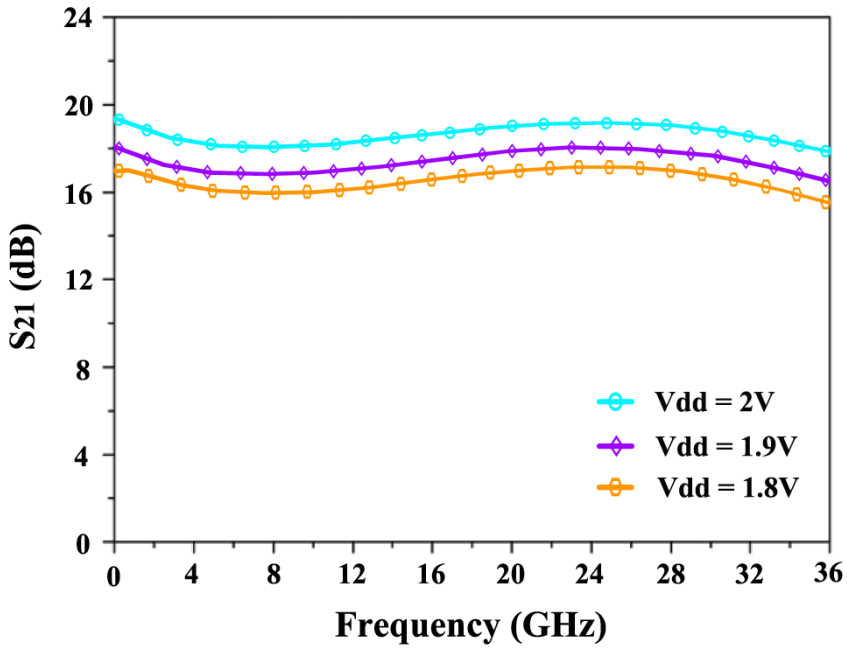

Figure 23. S_{21}'s response to power supply variations.

To evaluate the variations from the nominal simulation results, a linear process corner analysis was conducted at the slow–slow (SS) and fast–fast (FF) corners in Figures 24 and 25. It was observed that the NF fluctuates between 4.9 dB at the FF corner and 3.1 dB at the SS corner, with a nominal value of 3.7 dB. Meanwhile, the S_{21} reaches a minimum of 14.2 dB at the SS corner and a maximum of 19.8 dB at the FF corner, with a nominal value of 17.5 dB.

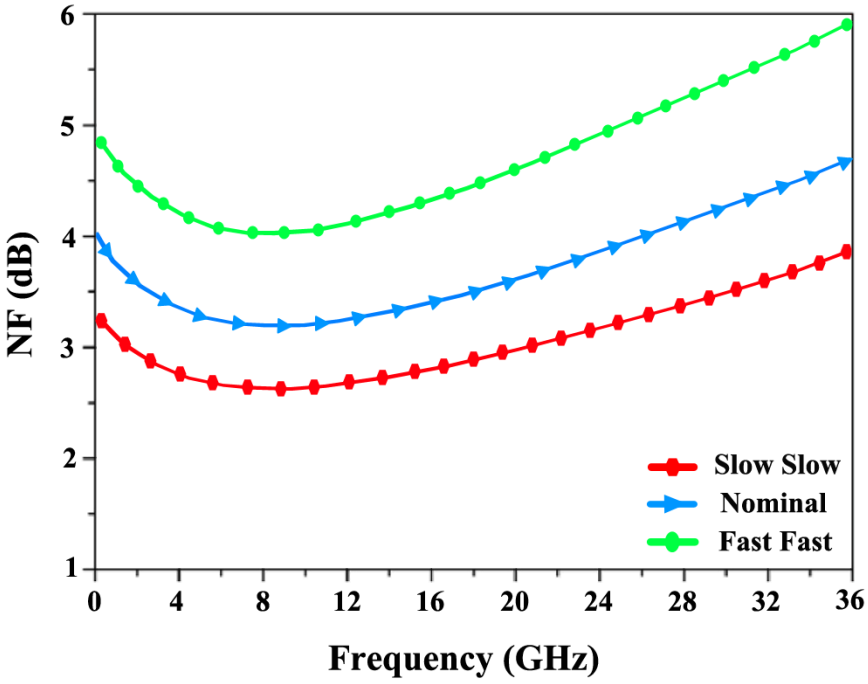

Figure 24. Corners simulations of nominal, slow–slow (SS), and fast–fast (FF) for NF.

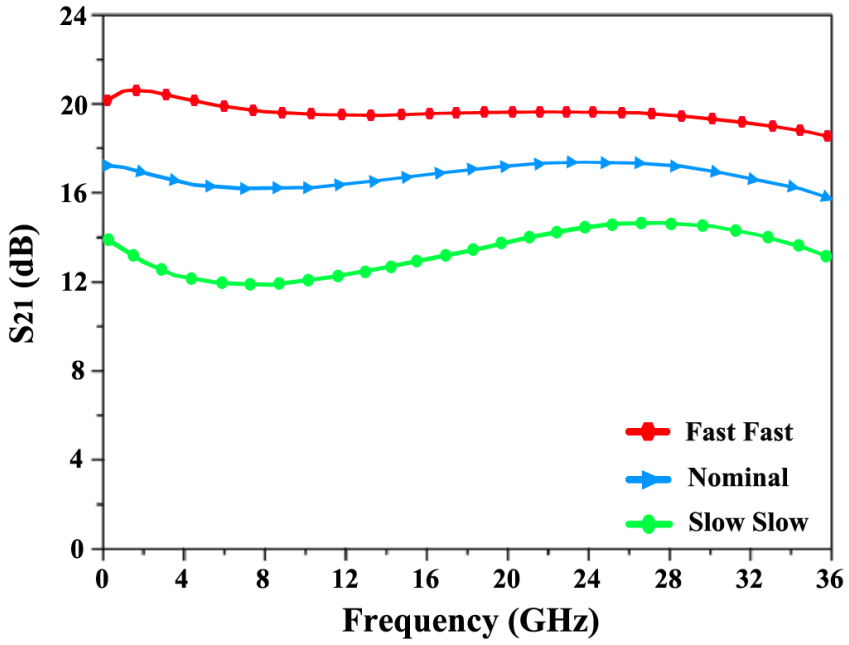

Figure 25. Corners simulations of nominal, slow–slow (SS), and fast–fast (FF) for S_{21}.

Figure 26 explores the influence of temperature fluctuations, ranging from −25 °C to 80 °C, on the NF and power gain (S_{21}) over the frequency range of 12 to 28 GHz. As the temperature rises, the NF increases, with a minimum of 4.9 dB at 80 °C and 3.1 dB at −25 °C. Additionally, the rise in temperature causes resistive components to consume more DC power, leading to a reduction in overall power gain. Figure 27 shows that S_{21} decreases from a maximum of 19.8 dB at −25 °C to a minimum of 14.2 dB at 80 °C.

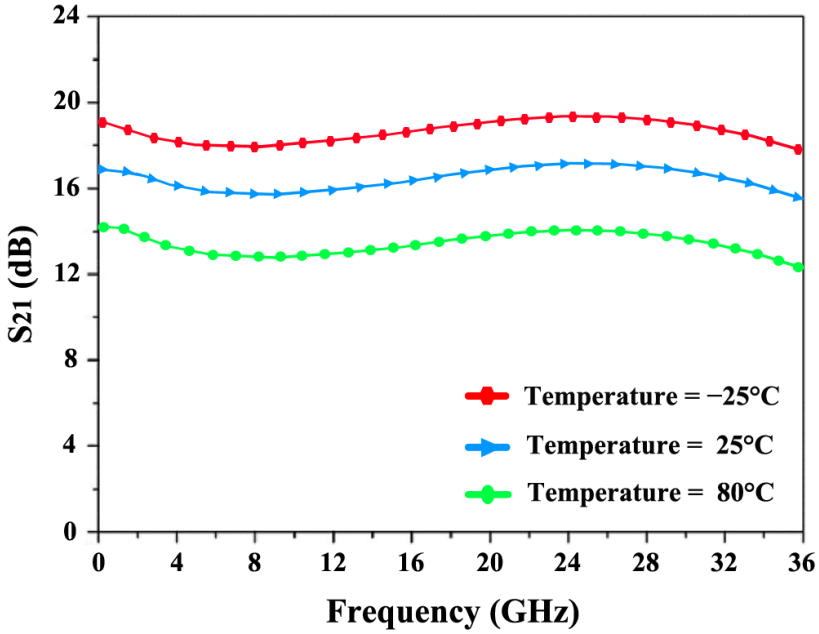

Figure 26. S_{21}'s response to temperature variations.

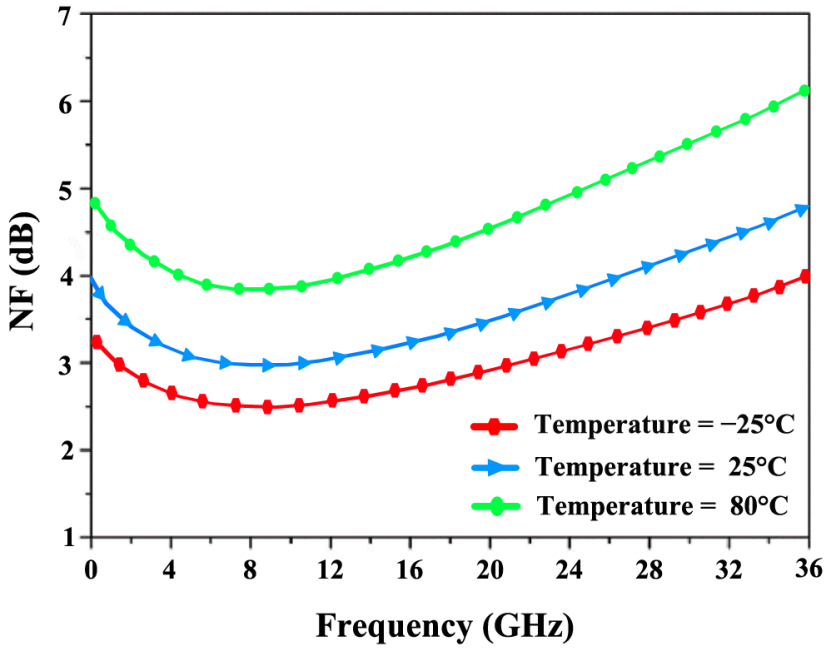

Figure 27. NF's response to temperature variations.

The histogram for the NF, generated after 10,000 trials in the Monte Carlo (MC) analysis, provides a statistical distribution of the NF values. This analysis allows for the observation of how NF varies across the trials, offering insights into the overall performance and consistency of the system under varying conditions. Figures 28 and 29 present the MC analysis, performed to assess the variations in NF and S_{21}, respectively. For the frequency range of 10–30 GHz, 100 iterations were conducted to evaluate the frequency response of NF and S_{21}, while the histogram plots of NF and S_{21} were generated after 10,000 trial runs. The MC analysis in Figure 28 reveals that 90.5% of the samples meet the requirements, with an NF below 3.7 dB after 10,000 trials. Additionally, Figure 29 shows that the mean NF is 4.33 dB with a standard deviation of 0.55 dB. As for S_{21}, the results in Figure 29 indicate that the mean power gain is 18.25 dB with a standard deviation of 1.32 dB after 10,000 trials.

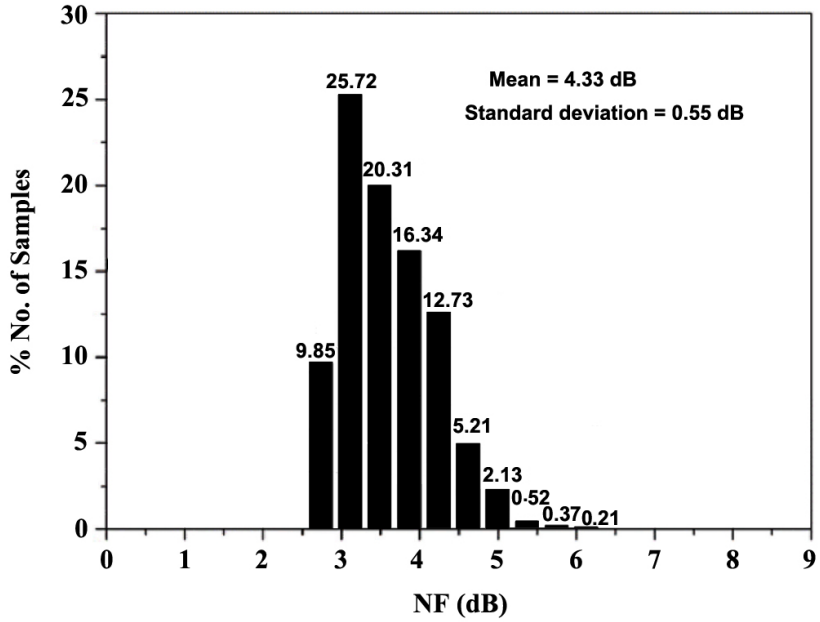

Figure 28. Monte Carlo analysis of NF.

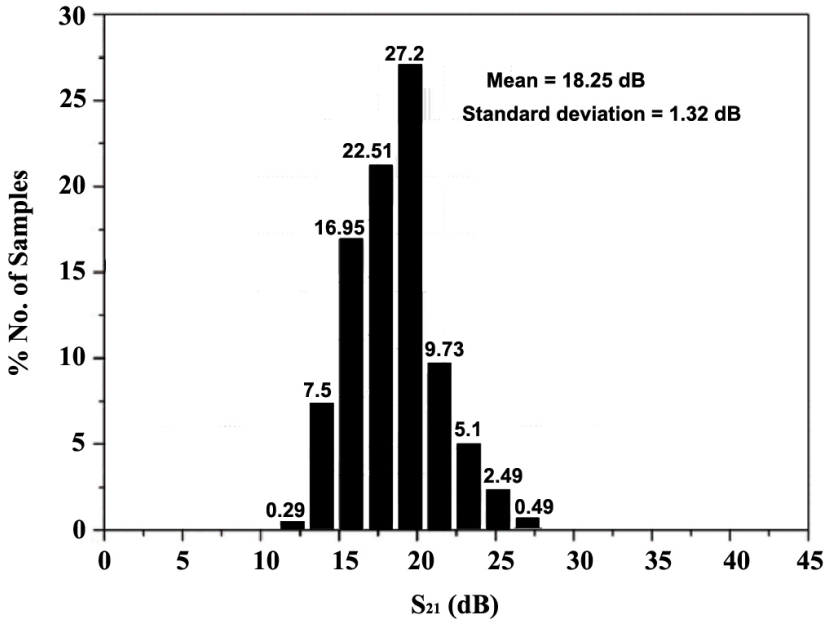

Figure 29. Monte Carlo analysis of S_{21}.

Layout Issues

Figure 30 depicts the chip photograph of the proposed LNA. The proposed LNA has been designed and fabricated using CMOS 65 nm technology. The inductive and capacitive parasitic effects have been attempted to be minimized by carefully laid out the compact chip layout. To reduce the transistors' series gate resistance and to avoid nonlinearity due to transistors' parasitic shunt capacitance, the layout of LNA transistors was designed with a 2 μm width per finger. Two fF/μm^2 metal–insulator–metal (MIM) capacitors were used in the LNA design, and a multilayer metal structure was used to minimize the inductance and resistance of the ground plane. The top metal layer, layer 9, was used to design the inductors with a quality factor (Q) of 13 at 24 GHz, and the output transformer was designed with a metal layer 8 and metal layer 9. The designed LNA chip die size was 0.67 mm^2. The Cadence Spectre RF simulator was used to calculate the post-layout results

of the designed LNA. The large-signal measurement of the LNA was achieved using the Agilent spectrum analyzer (PXA N9030 A) and Agilent signal generator (PSG 8257D). Small signal measurement was conducted by using the S parameter simulation technique, and it acquired specifications of LNA, which included gain, noise value, and reflection coefficient.

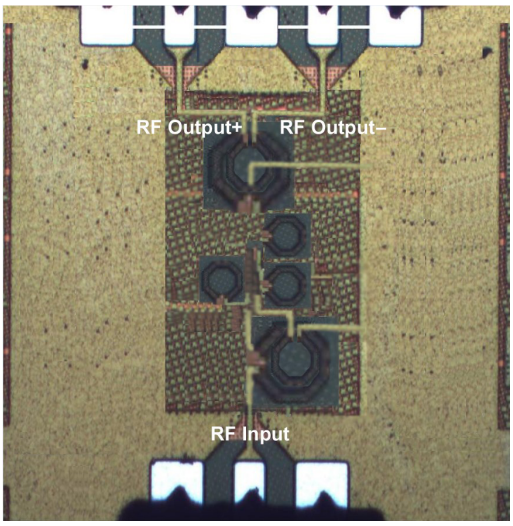

Figure 30. Chip photograph.

In Table 11, we summarize the performance characteristics of the other reported CMOS LNAs along with the proposed LNA.

Table 11. Performance characteristics of other reported CMOS LNAs.

Ref.	Tech (nm)	V_{DD} (V)	FrEquation (GHz)	S_{21} (dB)	NF (dB)	IP_1dB	Power (mW)
[36]	65 nm	1.5	60	11.289	1.819	N/A	7.25
[37]	180 nm	N/A	24	12.8	3.3	N/A	8
[38]	0.25 µm BiCMOS	1.8	16–43	10.5	2.5-4	1.8 (IIP3)	24
[39]	0.13 µm CMOS	12	27–31	22.14	1.86	−16 (IIP3)	33.4
[40]	45 nm	N/A	5.0–27.5	18.57 (PSO)	2.4–3.1	N/A	1.6
[41]	180 nm	1.8	5.5	22.15 (firefly)	1.16	−2.60 (IIP3)	N/A
[This Work]	65 nm	1.8	24	17.5/12.9 (sim./meas) (an-QNA)	3.7/4.98 (sim./meas) (an-QNA)	−13.1/−17.8 (sim./meas) (an-QNA)	28

5. Conclusions and Future Research

In conclusion, an-QNA method has been developed in this paper that significantly improves the performance of LNAs. Additionally, the proposed method accelerates convergence while improving linearity using I I_{PL} techniques and ensuring global convergence. A highly efficient LNA is designed to achieve enhanced performance using 65 nm CMOS technology, and as a result, achieves a simulated gain of 17.5 dB, an NF of 3.7 dB, as well as an (IP_1dB) of −13.1 dBm. The optimized an-QNA-based LNA includes a measured gain of 12.9 dB, a measured NF of 4.98 dB, and a measured compression point of the input 1 dB of −17.8 dB. The chip area of the optimized LNA is 0.67 mm^2. In automobile radar applications, these advancements demonstrate the potential of the an-QNA method. Future research could explore alternative CMOS nodes, such as 45 nm or 28 nm, that may enhance performance further. Moreover, further research is needed to optimize power consumption while maintaining performance, expand the frequency range, determine the robustness of

the LNA against variations in the processing process, and integrate the LNA with other components of the radar system.

Author Contributions: Conceptualization, U.A. and T.S.D.; methodology, U.A., L.S.W. and T.S.D.; validation, U.A. and A.S.; formal analysis, A.J., U.A. and A.S.; investigation Y.L. and T.S.D.; resources, Y.L. and J.-Y.R.; data curation, A.S. and Y.L.; writing—original draft preparation, A.S. and T.S.D.; writing—review and editing, Y.L. and J.-Y.R.; supervision, A.S., Y.L. and J.-Y.R.; funding acquisition, J.-Y.R. All authors have read and agreed to the published version of this manuscript.

Funding: We are thankful to the National Research Foundation (NRF) (2018R1D1A1B07043286) of Korea for sponsoring this research publication under Project BK21 FOUR (Smart Robot Convergence and Application Education Research Center).

Institutional Review Board Statement: Not applicable.

Informed Consent Statement: Not applicable.

Data Availability Statement: Data are contained within the article.

Acknowledgments: This research was supported by the Basic Science Research Program through the *National Research Foundation of Korea* (NRF) funded by the Ministry of Education. We are also thankful to the IC Design Education Center (IDEC), Korea, for their support for chip fabrication and EDA tools.

Conflicts of Interest: The authors declare no conflicts of interest.

References

1. As, D.E.; Yelten, M.B. A highly-linear, sub-mW LNA at 2.4 GHz in 40 nm CMOS process. *Integration* **2023**, *88*, 278–285.
2. Lin, H.T.; Gao, L.; Li, H.Y.; Xu, J.X.; Zhang, X.Y. A 23.6–46.5 GHz LNA with 3 dB NF and 24 dB Gain Tuning Range in 28-nm CMOS Technology. *IEEE Trans. Circuits Syst. I Regul. Pap.* **2023**, *71*, 29–39. [CrossRef]
3. Roobert, A.A.; Arunodhayamary, P.S.; Rani, D.G.N.; Venkatesh, M.; Julus, L.J. Design and analysis of 28 GHz CMOS low power LNA with 6.4 dB gain variability for 5G applications. *Trans. Emerg. Telecommun. Technol.* **2022**, *33*, e4486. [CrossRef]
4. Kalra, D.; Srivastava, M. Design and optimization of variable gain LNA for IoT applications using meta-heuristics search algorithms. *Microelectron. Eng.* **2024**, *286*, 112125. [CrossRef]
5. Kim, D.; Im, D. A reconfigurable balun-LNA and tunable filter with frequency-optimized harmonic rejection for sub-GHz and 2.4 GHz IoT receivers. *IEEE Trans. Circuits Syst. I Regul. Pap.* **2022**, *69*, 3164–3176. [CrossRef]
6. Pandey, R.J.; Raghava, N.S. Harmonic analysis of CMOS low noise amplifier with employing PMOS IMD technique for biosensor applications. *Microsyst. Technol.* **2023**, *29*, 875–898. [CrossRef]
7. Deng, Z.; Zhou, J.; Qian, H.J.; Luo, X. A 22.9–38.2-GHz dual-path noise-canceling LNA with 2.65–4.62-dB NF in 28-nm CMOS. *IEEE J. Solid-State Circuits* **2021**, *56*, 3348–3359. [CrossRef]
8. Seifi, Z.; Ghorbani, A.; Abdipour, A. Analysis and experimental study of radiative microwave pulses ef-fects on the nonlinear performance of a low-noise amplifier. *IEEE Trans. Plasma Sci.* **2021**, *49*, 1105–1114. [CrossRef]
9. Shen, C.; Zhao, P.; Luo, X. On energy efficient uplink multi-user mimo with shared lna con-trol. In Proceedings of the ICC 2021-IEEE International Conference on Communications, Montreal, QC, Canada, 14–23 June 2021; pp. 1–6.
10. Ibragimov, A.M.; Mikhailov, M.N.; Smirnov, E.P. Reducing odd-order nonlinear distortions in a low noise amplifier. In Proceedings of the 2023 5th International Youth Conference on Radio Electronics, Electrical and Power Engineering (REEPE), Moscow, Russia, 16–18 March 2023; Volume 5, pp. 1–5.
11. Younis, A.T.; Abdo, E.A. Low noise amplifier (LNA) performance optimization using genetic algorithms (GAS). *J. Eng. Sci. Technol.* **2020**, *15*, 3122–3131.
12. Bouali, H.; Benhala, B.; Guerbaoui, M. Multi-objective optimization of CMOS low noise amplifier through nature-inspired swarm intelligence. *Bull. Electr. Eng. Inform.* **2023**, *12*, 2824–2836. [CrossRef]
13. Dheerai, R.; Hiranmayee, K.B.; Praveena, K.S.; Dhanaraj, A.B.; Mallikarjuna, B.; Bhargavi, K. A Study on LNA, PLL and BPF of Front-End Integrated RF Receiver for Wireless Applications. In Proceedings of the 2021 6th International Conference on Communication and Electronics Systems (ICCES), Coimbatore, India, 8–10 July 2021; pp. 977–982.
14. Kalra, D.; Goyal, V.; Srivastava, M. LNA Parameters Optimization Using Firefly Algorithm. In Proceedings of the 2023 3rd International Conference on Advancement in Electronics & Communication Engineering (AECE), Ghaziabad, India, 23–24 November 2023; pp. 94–97.
15. Abi, S.; Bouyghf, H.; Benhala, B.; Raihani, A. An optimal design of a short-channel RF low noise amplifier using a swarm intelligence technique. In *Embedded Systems and Artificial Intelligence: Proceedings of the ESAI 2019, Fez, Morocco, 6–7 November 2019*; Springer: Singapore, 2019; pp. 143–153.

16. Bouali, H.; Benhala, B.; Bouyghf, H. Optimal Design of CMOS 0.18 µm Low Noise Amplifier using Multi-Objective Artificial Bee Colony Algorithm. *Int. J. Adv. Trends Comput. Sci. Eng.* **2020**, *9*, 69–75. [CrossRef]
17. Thakker, R.A.; Baghini, M.S.; Patil, M.B. Low-power low-voltage analog circuit design using hierarchical particle swarm optimization. In Proceedings of the IEEE 22nd International Conference on VLSI Design 2009, New Delh, India, 5–9 January 2009; pp. 427–432.
18. Fakhfakh, M.; Cooren, Y.; Sallem, A.; Loulou, M.; Siarry, P. Analog circuit design optimization through the particle swarm optimization technique. *Analog. Integr. Circuits Signal Process.* **2010**, *63*, 71–82. [CrossRef]
19. Tulunay, G.; Balkir, S.A. synthesis tool for CMOS RF low noise amplifiers. *IEEE Trans. CAD Integr. Circuits Syst.* **2008**, *21*, 977–982. [CrossRef]
20. Wen, W.; Yilong, L.; Jeffrey, S.F.; Yong, Z. Particle Swarm Optimization and Finite- Element Based Approach for Microwave Filter Design. *IEEE Trans. Magn.* **2005**, *41*, 1800–1803
21. Sad, C.; Michailidis, A.; Noulis, T.; Siozios, K. A Hybrid GA/ML-Based End-to-End Automated Methodology for Design Acceleration of Wireless Communications CMOS LNAs. *Electronics* **2023**, *12*, 2428. [CrossRef]
22. Liao, T.; Zhang, L. Efficient parasitic-aware hybrid sizing methodology for analog and RF integrated circuits. *Integration* **2018**, *62*, 301–313. [CrossRef]
23. Olenšek, J.; Bűrmen, Á.; Puhan, J.; Tuma, T. DESA: A new hybrid global optimization method and its application to analog integrated circuit sizing. *J. Glob. Optim.* **2009**, *44*, 53–77. [CrossRef]
24. Li, Y. A simulation-based evolutionary approach to LNA circuit design optimization. *Appl. Math. Comput.* **2009**, *209*, 57–67 [CrossRef]
25. Karkhanehchia, M.M.; Naderib, S.; Jafaria, F.; Majidifarc, S. Design and optimization of a very low noise amplifier using particle swarm optimization technique. *Int. J. Eng. Technol.* **2014**, *2*, 122–131
26. Shin, L.W.; Chin, N.S.; Marzuki, A. 5 GHz MMIC LNA design using particle swarm optimization. *Inf. Manag. Bus. Rev.* **2013**, *5*, 257–262
27. Papadimitriou, A.; Bucher, M. Multi-objective low-noise amplifier optimization using analytical model and genetic computation. *Circuits Syst. Signal Process.* **2017**, *36*, 4963–4993. [CrossRef]
28. Khong, S.Z.; Nešić, D.; Manzie, C.; Tan, Y. Multidimensional global extremum seeking via the DIRECT optimisation algorithm. *Automatica* **2013**, *49*, 1970–1978. [CrossRef]
29. Shams, M.; Rashedi, E.; Hakimi, A. Clustered-gravitational search algorithm and its application in parameter optimization of a low noise amplifier. *Appl. Math. Comput.* **2015**, *258*, 436–453. [CrossRef]
30. Konstantopoulos, G.; Papathanasiou, K.; Samelis, A. Optimization of RF circuits by expert monitored genetic computation. In Proceedings of the IEEE International Symposium on Circuits and Systems (ISCAS), Island of Kos, Greece, 21–24 May 2006; pp. 5247–5250.
31. Chen, H.-H.; Chen, M.-H.; Tsai, C.-Y. Optimization of low noise amplifier designs by genetic algorithms. In Proceedings of the International Symposium on Electromagnetic Theory (EMTS), Hiroshima, Japan, 20–23 May 2013; pp. 493–496.
32. Dutta, A.; Dasgupta, K.; Bhattacharyya, T.K. Compact small signal modeling and PSO-based input matching of a packaged CMOS LNA in subthreshold region. *Microelectron. J.* **2007**, *38*, 1050–1056. [CrossRef]
33. Jiang, Z.; Liu, Z.; Liu, H.; Zhao, C.; Wu, Y.; Kang, K. A 24 GHz enhanced neutralized cascode LNA with 4.7 dB NF and 19.8 dB gain. *IEICE Electron. Express* **2018**, *15*, 20180464. [CrossRef]
34. Suganthi, K.; Malarvizhi, S. Millimeter wave CMOS minimum noise amplifier for automotive radars in the frequency band (60–66 GHZ). *Clust. Comput.* **2019**, *22* (Suppl. 5), 11755–11764. [CrossRef]
35. Zhang, H.; Sánchez-Sinencio, E. Linearization techniques for CMOS low noise amplifiers: A tutorial. *IEEE Trans. Circuits Syst. I Regul. Pap.* **2010**, *58*, 22–36. [CrossRef]
36. Fan, X.; Sánchez-Sinencio, E.; Silva-Martinez, J. A 3 GHz–10 GHz common gate ultrawideband low noise amplifier. In Proceedings of the IEEE Midwest Symposium Circuits and Systems, Cincinnati, OH, USA, 7–10 August 2005; pp. 631–634.
37. Shin, S.; Tsai, M.; Liu, R.; Lin, K.; Wang, H. A 24-GHz 3.9-dB NF low-noise amplifier using 0.18 CMOS technology. *IEEE Microw. Wireless Compon. Lett.* **2005**, *15*, 448–450. [CrossRef]
38. Chen, Z.; Gao, H.; Leenaerts, D.; Milosevic, D.; Baltus, P. A 29–37 GHz BiCMOS low-noise amplifier with 28.5 dB peak gain and 3.1–4.1 dB NF. In Proceedings of the 2018 IEEE Radio Frequency Integrated Circuits Symposium (RFIC), Philadelphia, PA, USA, 10–12 June 2018; IEEE: Piscataway, NJ, USA, 2018; pp. 288–291.
39. Hosseini, S.A.; Taheri, M.M.; Khosravi, R.; Moradi, G. A 27–31 GHz CMOS LNA for 5G Application via Improved Noise Cancellation Technique and Gain Boosting. *Int. J. Smart Electr. Eng.* **2022**, *11*, 21–26
40. Kumar, M.; Deolia, V.K. Performance analysis of low power LNA using particle swarm optimization for wide band application. *AEU-Int. J. Electron. Commun.* **2019**, *111*, 152897. [CrossRef]
41. Kumar, R.; Talukdar, F.A.; Rajan, A.; Devi, A.; Raja, R. Parameter optimization of 5.5 GHz low noise amplifier using multi-objective Firefly Algorithm. *Microsyst. Technol.* **2020**, *26*, 3289–3297. [CrossRef]